Modeling the Microstructure and Stress in Dense Suspensions under Inhomogeneous Flow

J. J. J. Gillissen[1,*] and C. Ness[2]

[1]*Department of Mathematics, University College London, Gower Street, London WC1E 6BT, United Kingdom*
[2]*School of Engineering, University of Edinburgh, Edinburgh EH9 3FB, United Kingdom*

Under inhomogeneous flow, dense suspensions exhibit behavior that violates the conventional homogeneous rheology. Specifically, one finds flowing regions with a macroscopic friction coefficient below the yielding criterion, and volume fraction above the jamming criterion. We demonstrate the underlying physics by incorporating shear rate fluctuations into a recently proposed tensor model for the microstructure and stress, and applying the model to an inhomogeneous flow problem. The model predictions agree qualitatively with particle-based simulations.

Introduction.—Many materials, such as foods, cosmetics, and ceramic precursors, consist of particles densely suspended in liquid, and their production relies on understanding the corresponding fluid mechanics [1]. Despite a century of intense research including recent progress [2], comprehensive theoretical models are still lacking [3]. Indeed, even the simple case of non-Brownian, noninertial, hard spheres remains deceptively challenging [4]. Under simple shear flow the mechanics are, in principle, governed by a single dimensionless parameter: specifying only the macroscopic friction coefficient $\mu = \Sigma_{xy}/\Pi$ sets the remaining nondimensional variables, viz., the volume fraction ϕ and the nondimensional shear rate $S = \eta_s \dot{\gamma}/\Pi$ [5]. Here, Σ_{xy} is the shear component of the stress tensor Σ_{ij}, $\Pi = -D^{-1}\Sigma_{ii}$ is the pressure (in D dimensions), η_s is the viscosity of the suspending medium, and $\dot{\gamma}$ is the shear rate. Carefully designed homogeneous flow experiments support this picture, revealing a decreasing S and increasing ϕ upon reducing μ, until the system jams ($S = 0$) when ϕ reaches a maximum and μ reaches a minimum value [5]. As opposed to frictionless particles that jam isotropically at random close packing $\phi = \phi_{\mathrm{RCP}}$ and $\mu = 0$, frictional particles jam with an anisotropic microstructure at $\phi = \phi_J < \phi_{\mathrm{RCP}}$ and $\mu = \mu_J > 0$ [6].

Despite the conceptual power of this general result [4], its utility beyond homogeneous shear is limited. In pressure driven Poiseuille flow, for example, momentum conservation dictates that $\mu < \mu_J$ in a finite region around the center line. In this region, the $[S(\mu), \phi(\mu)]$ rheology described above clearly predicts jamming with $S = 0$ and $\phi = \phi_J$. This behavior is not observed in experiments and particle-based simulations, however, which instead consistently show "subyielding" ($S > 0$) and sometimes "overcompaction" ($\phi > \phi_J$), in regions where $\mu < \mu_J$ [7–11]. Making quantitative predictions of practical flows that comprise contiguous regions of $\mu > \mu_J$ and $\mu < \mu_J$ thus requires more detailed constitutive models that capture both

homogeneous rheology *and* the physics of subyielding and overcompaction that arise under inhomogeneous conditions. Although these effects have been addressed separately in the literature, there are no models available that capture both effects simultaneously.

Subyielding and overcompaction under inhomogeneous flow occur in regions of vanishing shear rate, where the dynamics are completely governed by fluctuating particle motions [12–21]. These fluctuations propagate from flowing regions with $\mu > \mu_J$ into (nearly solid) regions with $\mu < \mu_J$, inducing particle rearrangements. This may allow the suspension to fluidize in otherwise solid regions, with $\phi_J < \phi < \phi_{\mathrm{RCP}}$.

Attempts at incorporating overcompaction in constitutive models are so far limited to linear extrapolation of the homogeneous $\phi(\mu)$ relation from regions with $\mu > \mu_J$ into regions with $\mu < \mu_J$ [20]. The shape of the resulting density profiles, however, qualitatively differs from experimental data [7,8,11]. Subyielding, meanwhile, has been modelled by subjecting the fluidity (inverse viscosity) to a diffusion process [18], or by accounting for fluctuations in the expression for the suspension stress, with the fluctuation magnitude being computed using a transport equation borrowed from kinetic theory [9]. Alternatively, a simpler account for fluctuations can be derived by spatially averaging, i.e., filtering, the stress over a volume that is small compared to the system size and large compared to the particle size [12,22,23]. This leads to an increase in the normal viscosity but leaves the shear viscosity unaffected, thereby reducing μ below μ_J. Crucially, these subyielding models fail to account for microstructural changes due to fluctuations and therefore do not capture overcompaction.

In this Letter, we address these shortcomings, providing an intuitive explanation of subyielding and overcompaction. We do so by incorporating shear rate fluctuations into a recent microstructure model [24–28]. When applied to

inhomogeneous flows the resulting tensorial constitutive model predicts that fluctuations can (i) isotropize the microstructure; (ii) increase ϕ above ϕ_J; (iii) reduce μ below μ_J. We compare the model predictions to those of particle-based simulations.

Constitutive model.—The suspension stress tensor is modeled as [28]

$$\frac{\boldsymbol{\Sigma}}{\eta_s} = 2\langle \boldsymbol{E} \rangle + \left[\frac{\alpha_0 \langle \boldsymbol{E} \rangle}{\left(1 - \frac{\phi}{\phi_{\mathrm{RCP}}}\right)^2} + \frac{\chi_0 \langle \boldsymbol{E}_c \rangle}{\left(1 - \frac{\xi}{\xi_J}\right)^2} \right] : \langle \boldsymbol{nnnn} \rangle. \quad (1)$$

Here, $\boldsymbol{n}$ is the separation unit vector of interacting particle pairs, $\boldsymbol{L} = \nabla \boldsymbol{u}^T$ is the velocity gradient tensor, and $\boldsymbol{E} = \frac{1}{2}(\boldsymbol{L} + \boldsymbol{L}^T)$ is the rate of strain tensor, which we decompose into extensional $\boldsymbol{E}_e$ and compressive $\boldsymbol{E}_c$ parts:

$$\boldsymbol{E}_e = \frac{1}{2}\boldsymbol{E} + \frac{1}{4}||\boldsymbol{E}||\boldsymbol{\delta}, \qquad \boldsymbol{E}_c = \frac{1}{2}\boldsymbol{E} - \frac{1}{4}||\boldsymbol{E}||\boldsymbol{\delta}. \quad (2)$$

Note that Eq. (2) is valid in 2D but not in 3D. Given the practical ubiquity of 2D shear we nonetheless proceed with Eq. (2).

In Eq. (1) the filter operator $\langle \cdot \rangle$ averages over particle pairs that are contained in a space-time, *filtering* volume which must be small compared to the spatial and temporal extents of the suspension and large compared to those of the fluctuations. When carrying out the filtering, it has been assumed in Eq. (1) [and in Eq. (5) below] that the fluctuations in the velocity gradient field are uncorrelated with the fluctuations in the pair separation vector, e.g., $\langle \boldsymbol{E}_c \boldsymbol{nnnn} \rangle \approx \langle \boldsymbol{E}_c \rangle \langle \boldsymbol{nnnn} \rangle$.

In Eq. (1) the jamming coordinate ξ is defined as [28]

$$\xi = -\frac{\langle \boldsymbol{nn} \rangle : \langle \boldsymbol{E}_c \rangle}{\sqrt{\langle \boldsymbol{E}_c \rangle : \langle \boldsymbol{E}_c \rangle}}, \quad (3)$$

which acts as a proxy for the coordination number Z, i.e., the number of direct contacts per particle [27]. The first and second terms in Eq. (1) are, respectively, the stress induced by the fluid and by the particles. The latter contains lubrication and contact contributions, where α_0 and χ_0 are constants and ξ_J is the value of ξ at jamming.

In Eq. (1) the fourth-order moment $\langle \boldsymbol{nnnn} \rangle$ of the orientation distribution function of $\boldsymbol{n}$ is expressed in terms of the second-order moment $\langle \boldsymbol{nn} \rangle$ using [29]:

$$\langle n_i n_j n_k n_l \rangle = -\langle n_m n_m \rangle$$
$$\times \frac{1}{(D+2)(D+4)} (\delta_{ij}\delta_{kl} + \delta_{ik}\delta_{jl} + \delta_{il}\delta_{jk})$$
$$+ \frac{1}{D+4} (\delta_{ij}\langle n_k n_l \rangle + \delta_{ik}\langle n_j n_l \rangle + \delta_{il}\langle n_j n_k \rangle)$$
$$+ \langle n_i n_j \rangle \delta_{kl} + \langle n_i n_k \rangle \delta_{jl} + \langle n_i n_l \rangle \delta_{jk}). \quad (4)$$

The second-order moment $\langle \boldsymbol{nn} \rangle$ is related to the velocity gradient field with the following steady state balance equation [28]:

$$0 = \langle \boldsymbol{L} \rangle \cdot \langle \boldsymbol{nn} \rangle + \langle \boldsymbol{nn} \rangle \cdot \langle \boldsymbol{L}^T \rangle - 2\langle \boldsymbol{L} \rangle : \langle \boldsymbol{nnnn} \rangle$$
$$- \beta \left[\langle \boldsymbol{E}_e \rangle : \langle \boldsymbol{nnnn} \rangle + \frac{\phi}{D(D+2)} (2\langle \boldsymbol{E}_c \rangle + \mathrm{Tr}(\langle \boldsymbol{E}_c \rangle)\boldsymbol{\delta}) \right]. \quad (5)$$

The "pair association rate" β controls the rate at which particle pairs are created and destroyed by fluid compression and extension, set, respectively, by $\boldsymbol{E}_c$ and $\boldsymbol{E}_e$. Equations (1)–(5) define a constitutive model for steady microstructure and stress in dense suspensions.

Incorporating fluctuations.—The shear rate consists of a mean $\dot{\gamma} = ||\langle \boldsymbol{E} \rangle|| = \sqrt{2\langle \boldsymbol{E} \rangle : \langle \boldsymbol{E} \rangle}$ and fluctuations. While in homogeneous flow the fluctuations are subdominant to the mean, the fluctuations may dominate the mean in inhomogeneous flow, e.g., close to a Poiseuille center line. In those regions, although the filtered $\boldsymbol{E}$ is (nearly) zero, the filtered $\boldsymbol{E}_e$ and $\boldsymbol{E}_c$ are nonzero, which is a consequence of the nonlinearity of $\boldsymbol{E}_e$ and $\boldsymbol{E}_c$ in $\boldsymbol{E}$ [Eq. (2)]. Below we account for fluctuations in the model [Eqs. (1)–(5)] by filtering $\boldsymbol{E}_e$ and $\boldsymbol{E}_c$.

In order to express $\langle \boldsymbol{E}_e \rangle$ and $\langle \boldsymbol{E}_c \rangle$ in terms of $\langle \boldsymbol{E} \rangle$, we use that a fluctuating quantity $q = \langle q \rangle + q'$ can be decomposed into its filtered $\langle q \rangle$ and its fluctuating q' components, and that $\langle q' \rangle = 0$. Filtering a nonlinear function of q gives additional terms. Specifically, filtering the absolute value of q gives $\langle |\langle q \rangle + q'| \rangle \approx |\langle q \rangle| + q_{\mathrm{rms}}$ [30] where $q_{\mathrm{rms}} = \langle |q'| \rangle$. Similarly, filtering Eq. (2) gives

$$\langle \boldsymbol{E}_e \rangle = \langle \boldsymbol{E} \rangle_e + \frac{1}{4}\dot{\gamma}_{\mathrm{rms}}\boldsymbol{\delta}, \qquad \langle \boldsymbol{E}_c \rangle = \langle \boldsymbol{E} \rangle_c - \frac{1}{4}\dot{\gamma}_{\mathrm{rms}}\boldsymbol{\delta}, \quad (6)$$

where $\dot{\gamma}_{\mathrm{rms}} = \langle ||\boldsymbol{E}'|| \rangle$ is the amplitude of the shear rate fluctuations.

In homogeneous shear flow, the fluctuating shear rate $\dot{\gamma}_{\mathrm{rms}}$ vanishes when the mean shear rate $\dot{\gamma}$ vanishes. In inhomogeneous shear flows, on the other hand, $\dot{\gamma}_{\mathrm{rms}}$ may remain finite when $\dot{\gamma} \to 0$, since fluctuations are propagating from nearby regions with finite $\dot{\gamma}$. In this limiting case, the dynamics are dominated by $\dot{\gamma}_{\mathrm{rms}}$ and $\langle \boldsymbol{E}_e \rangle = -\langle \boldsymbol{E}_c \rangle = \frac{1}{4}\dot{\gamma}_{\mathrm{rms}}\boldsymbol{\delta}$. Inserting these expressions into the filtered microstructure and stress equations [Eqs. (1), (4), and (5)] gives isotropic tensors for the microstructure $\langle \boldsymbol{nn} \rangle \sim \boldsymbol{\delta}$ and the stress $\boldsymbol{\Sigma} \sim -\eta_s \dot{\gamma}_{\mathrm{rms}}\boldsymbol{\delta}$, with negative normal stresses and zero shear stresses. This behavior corresponds to a vanishing macroscopic friction coefficient μ, below the jamming friction coefficient for homogeneous systems μ_J. Our constitutive model similarly predicts isotropization of the microstructure and stress in shear flow with superposed shear oscillations [28].

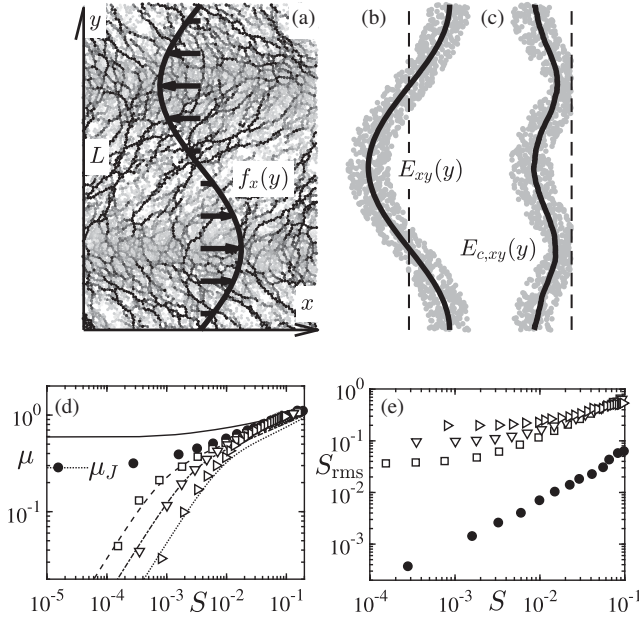*Kolmogorov flow.*—We apply the above model [Eqs. (1)–(6)] to steady 2D Kolmogorov flow, driven by

FIG. 1. (a) Snapshot of particle-based simulation of Kolmogorov flow with relative domain size $L/a = 278$. The gray level indicates the particle pressure (black and white represent negative and positive, respectively) and the driving force $f_x(y)$ is sketched with the black line. (b),(c) Sketches of the xy component of E and E_c respectively, showing raw signals (gray) and filtered signals (black). The latter is zero at $y/L = 0.25, 0.75$ for $\langle E \rangle$ but not for $\langle E_c \rangle$. The dashed lines indicate the abscissas. (d) Macroscopic friction coefficient μ as a function of the nondimensional shear rate S predicted by simulation in homogeneous shear flow (filled circles) and in Kolmogorov flow for $L/a = 278$ (open squares), 139 (open downward triangles), and 56 (open rightward triangles) and predicted by constitutive model for $S_{rms} = 0$ (solid line) 6×10^{-3} (dashed line), 1.5×10^{-2} (dash-dotted line) and 4.2×10^{-2} (dotted line). (e) Nondimensional shear rate fluctuations S_{rms} as a function of S predicted by simulation. The markers are as in (d).

a body force density $\boldsymbol{f} = \hat{f} \sin(2\pi y/L)\boldsymbol{\delta}_x$ (with $\hat{f}$ the force amplitude) pointing in the x direction and oscillating in the y direction with a wavelength L [Fig. 1(a)]. We chose this flow to test our model, as it is possibly the simplest inhomogeneous shear flow without solid surfaces. In this inhomogeneous shear flow $\boldsymbol{L} = \partial_y u_x \boldsymbol{\delta}_x \boldsymbol{\delta}_y$ and the fluid mechanical profiles are periodic in y and independent of x and t. Figures 1(b) and 1(c) show schematically the instantaneous and filtered profiles of the flow-gradient xy component of the total deformation $\boldsymbol{E}$ and of its compressive part $\boldsymbol{E}_c$. Crucially, the filtered $E_{xy} = 0$ on the center lines [at $y = L/4 \pmod{L/2}$], whereas the filtered $E_{c,xy} < 0$. This difference arises due to the nonlinearity of $\boldsymbol{E}_c$ in $\boldsymbol{E}$ mentioned above, and demonstrates that fluctuations produce normal stresses but no shear stresses, resulting in subyielding close to the center lines.

Particle-based simulation.—We compare our constitutive model to particle-based simulations on 2D domains

with dimensions in the x and y directions, respectively, of $L_x = 200a$ and $L = 56a$, $139a$, and $278a$. We use $N \sim 10^4$ bidisperse frictional spheres (radii a and $1.4a$, stiffness k, density ρ) and a domain averaged volume fraction:

$$\bar{\phi} = L^{-1} \int_0^L \phi(y)dy, \qquad (7)$$

of $\bar{\phi} = 0.7$. The particles interact with each other through short-range lubrication and frictional contact forces [31] while drag forces between the particles and the suspending medium are omitted. Instead, the flow is driven by a y-dependent force in the x direction $f_0 \sin(2\pi y/L)\boldsymbol{\delta}_x$ added to each particle. We set $f_0/ka = 10^{-8}$, sufficiently small for the particles to behave as hard, inertia-free spheres ($\rho\dot{\gamma}a^2/\eta_s < 10^{-2}$). The resulting driving force density is $\boldsymbol{f} = f_0 n(y) \sin(2\pi y/L)\boldsymbol{\delta}_x$ where $n(y)$ is the particle number density and the average force amplitude equals $\hat{f} = f_0 \bar{n} = f_0 N/(LL_x)$. Simulations are run until a statistically steady state is reached in the entire domain and profiles are computed thereafter over $\dot{\gamma}t \approx 20$, based on the maximum $\dot{\gamma}$ in the domain. We obtain velocity and structural profiles by averaging particle properties in y bins, so that each single simulation provides a range of μ and S values.

We also simulate 2D homogeneous shear flow, driven by Lees-Edwards boundary conditions, on a square domain with size $L = 56a$ and with $\phi = 0.5$–0.9. By measuring the divergence of the stresses with increasing ϕ, we found the jamming friction coefficient to be $\mu_J = 0.285$ and the limiting volume fractions as $\phi_J = 0.795$ and $\phi_{RCP} = 0.840$.

Model predictions of $\mu(S)$.—Figure 1(d) shows the simulation results on (S, μ) coordinates under homogeneous shear and in Kolmogorov flow for various L/a. The data points correspond to fixed ϕ values in homogeneous shear and to fixed y coordinates in the Kolmogorov simulation. The inhomogeneous Kolmogorov flow simulation predicts subyielding, i.e., $S > 0$ in regions where $\mu < \mu_J$ while the homogeneous shear simulation predicts the homogeneous $\mu(S)$ rheology consistent with Ref. [5].

Shown in Fig. 1(e) are the simulated, nondimensional shear rate fluctuations $S_{rms} = \eta_s \dot{\gamma}_{rms}/\Pi$ as a function of S for the same cases as in Fig. 1(d). The shear rate fluctuations $\dot{\gamma}_{rms} = \langle |\partial_y u'_x| \rangle$ are calculated based on instantaneous, local realizations of $\partial_y u_x$, computed by fitting a linear function to the spatial distribution of the instantaneous particle velocities in a box of size $6a$. The data show an increase in S_{rms} with a decrease in L/a (that is, for steeper gradients of the driving force) and a (non)vanishing S_{rms} in the limit of $S \to 0$ for the (in)homogeneous shear flow.

Constitutive model predictions are plotted with lines in Fig. 1(d), with $\alpha_0 = \chi_0 = 0.96$, $\xi_J = 0.6$, and $\beta = 4$. The latter two are not fitting parameters *per se*, but follow from
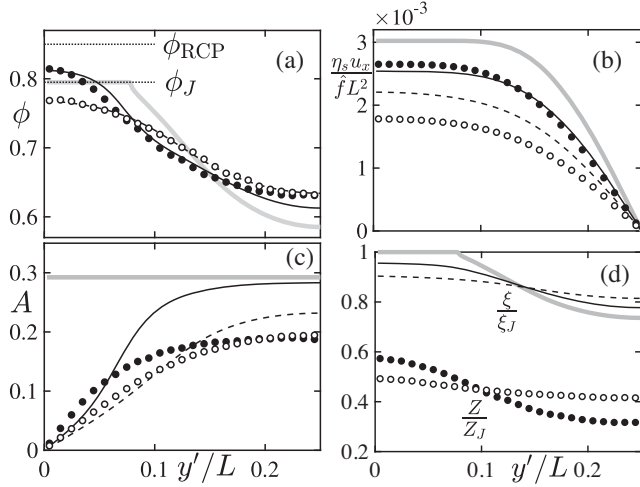
FIG. 2. Kolmogorov flow profiles as a function of the normalized distance to the nearest center line y'/L, predicted by constitutive model with $S_{rms} = 0$ (gray lines), $S_{rms} = 10^{-2}$ (solid black lines), and $S_{rms} = 10^{-1}$ (dashed black lines) and by simulations with $L/a = 278$ (filled circles) and 56 (open circles). (a) Volume fraction ϕ; (b) normalized velocity $u_x/(\hat{f}L^2/\eta_s)$; (c) anisotropy of particle contacts A; (d) normalized coordination number Z/Z_J in simulation and normalized jamming coordinate ξ/ξ_J in constitutive model.

$\phi_{RCP} = 0.840$ and $\phi_J = 0.795$ [32]. Each line is obtained by solving ϕ and S from Eqs. (1)–(6) for various values of μ at fixed S_{rms}. S_{rms} values are chosen to best match the simulation data in Fig. 1(d) (markers). They are somewhat smaller than S_{rms} predicted by simulation [Fig. 1(e)], reflecting that the constitutive model does not capture the correct quantitative relationship between μ, S, and S_{rms}. Nevertheless, the model predicts the correct qualitative behavior, specifically $S_{rms} > 0$ results in subyielding, i.e., $\mu \to 0$ as $S \to 0$, with the effect being amplified as S_{rms} is increased.

Model predictions of profiles.—Next, we make predictions of the velocity and structural profiles in Kolmogorov flow by combining our constitutive model [Eqs. (1)–(6)] with the (inertia-free) momentum balance $\boldsymbol{\nabla} \cdot \boldsymbol{\Sigma} + \boldsymbol{f} = \boldsymbol{0}$, whose x and y components reduce to

$$\Sigma_{xy} = \frac{\hat{f}L}{2\pi}\cos(2\pi y/L), \qquad \Sigma_{yy} = -\text{constant.} \quad (8)$$

We use three nondimensional shear rate fluctuations (assumed constant throughout the domain) $S_{rms} = 0$, 10^{-2}, and 10^{-1} where the former represents the homogeneous flow model and the latter two are chosen to match the model to the simulated ϕ profiles in Fig. 2(a) (described below). These S_{rms} values are different from those used in Fig. 1(d) which were chosen to match the simulated $\mu(S)$ profiles. These differences again indicate the quantitative discrepancies between model and simulation. We compute ϕ, $\partial_y u_x$, and $\langle \boldsymbol{nn} \rangle$ in each y coordinate for a given constant

Σ_{yy} from Eqs. (1)–(6), (8) using Newton-Raphson and then iteratively updating Σ_{yy} using the bisection method such that the integral volume fraction $\bar{\phi}$ [Eq. (7)] approaches 0.7.

Shown in Fig. 2 are profiles of the volume fraction ϕ [Fig. 2(a)], the nondimensional suspension velocity $u_x \eta_s/(\hat{f}L^2)$ [Fig. 2(b)], the anisotropy A of the particle contacts [Fig. 2(c)] and the coordination number Z normalized by the value at homogeneous jamming Z_J [Fig. 2 (d)]. Z is computed from the simulation output by counting contacting particle pairs (with $Z_J = 3$), while A is obtained by averaging $n_x n_y$ over all such pairs (with $\boldsymbol{n}$ the unit vector along the center-to-center line). In the constitutive model, Z/Z_J and A are represented, respectively, by ξ/ξ_J and $-(\langle \boldsymbol{E}_c \rangle : \langle \boldsymbol{nnnn} \rangle)_{xy}/\langle \boldsymbol{nn} \rangle : \langle \boldsymbol{E}_c \rangle$ [28]. Because of symmetry Fig. 2 only shows the profiles over one quarter of the wavelength L.

Without fluctuations, i.e., following the homogeneous rheology, the constitutive model predicts a jammed region around the center lines with $\dot{\gamma} = S = 0$ and $\phi = \phi_J$ (gray lines in Fig. 2). Fluctuations induce two effects. The first is an increase of the repulsive normal stress relative to the imposed shear stress, which is evidenced by a decrease in μ for small S in Fig. 1(d). This increased normal stress drives particles away from the center lines to the outer regions [Fig. 2(a)]. In these outer regions the shear rate is larger and the particles generate more shear stress than in the center line regions. This results in a lower nondimensional velocity [Fig. 2(b)]. The second effect is isotropization (i.e., $A \to 0$) of the microstructure [Fig. 2(c)], resulting in fewer particle contacts at a given ϕ [Fig. 2(d)]. This isotropization allows ϕ to exceed ϕ_J and *reduces* the normal stress near the center lines. These two competing effects may lead either to an increase in the volume fraction ϕ above ϕ_J (overcompaction, observed for $S_{rms} = 10^{-2}$) or to a reduction below ϕ_J (observed for $S_{rms} = 10^{-1}$) at the center lines [Fig. 2(a)].

Despite the qualitative agreement, there are quantitative differences between the constitutive model and the particle-based simulation. Figure 2(d), for instance, shows that ξ/ξ_J in the constitutive model is larger than Z/Z_J in the simulation. There are many possible avenues for improving the quantitative accuracy of the model, e.g., by relaxing the assumption that velocity gradient fluctuations are uncorrelated with microstructure fluctuations or by using complex relationships between the material functions α_0, χ_0, and β and the state variables ϕ, $\langle \boldsymbol{L} \rangle$, and $\langle \boldsymbol{nn} \rangle$. However, having demonstrated that our model contains a (possibly minimal) set of physics that can simultaneously reproduce subyielding and overcompaction, we have chosen mathematical simplicity over quantitative accuracy, leaving the above developments as promising routes for further analysis.

Conclusion.—We have presented a tensorial model for the microstructure and stress in dense suspensions of frictional particles that includes the effect of fluctuations by applying a filtering to the microstructure balance

equation. In doing so, we are able to predict subyielding and overcompaction, features common under practical flows but not predicted by homogeneous rheology models.

In addition to the potential model developments described above, further improvements to the predictive capacity for practical applications will require testing in complex geometries. We provide one such example in the Supplemental Material [33], namely, a comparison between model and simulation predictions for pressure driven flow through a curved channel. Addressing the full details of this and other complex flows will be the next step toward a comprehensive fluid dynamical description of dense suspensions.

---

[*] jurriaangillissen@gmail.com

[1] J. J. Stickel and R. L. Powell, Fluid mechanics and rheology of dense suspensions, Annu. Rev. Fluid Mech. **37,** 129 (2005).

[2] A. S. Baumgarten and K. Kamrin, A general constitutive model for dense, fine-particle suspensions validated in many geometries, Proc. Natl. Acad. Sci. U.S.A. **116,** 20828 (2019).

[3] M. M. Denn and J. F. Morris, Rheology of non-Brownian suspensions, Annu. Rev. Chem. Biomol. Eng. **5,** 203 (2014).

[4] É. Guazzelli and O. Pouliquen, Rheology of dense granular suspensions, J. Fluid Mech. **852** (2018).

[5] F. Boyer, É. Guazzelli, and O. Pouliquen, Unifying Suspension and Granular Rheology, Phys. Rev. Lett. **107,** 188301 (2011).

[6] M. Wyart and M. E. Cates, Discontinuous Shear Thickening without Inertia in Dense Non-Brownian Suspensions, Phys. Rev. Lett. **112,** 098302 (2014).

[7] R. E. Hampton, A. A. Mammoli, A. L. Graham, N. Tetlow, and S. A. Altobelli, Migration of particles undergoing pressure-driven flow in a circular conduit, J. Rheol. **41,** 621 (1997).

[8] M. K. Lyon and L. G. Leal, An experimental study of the motion of concentrated suspensions in two-dimensional channel flow. Part 1. Monodisperse systems, J. Fluid Mech. **363,** 25 (1998).

[9] P. R. Nott and J. F. Brady, Pressure-driven flow of suspensions: Simulation and theory, J. Fluid Mech. **275,** 157 (1994).

[10] K. Yeo and M. R. Maxey, Numerical simulations of concentrated suspensions of monodisperse particles in a Poiseuille flow, J. Fluid Mech. **682,** 491 (2011).

[11] S. Oh, Y.-q. Song, D. I. Garagash, B. Lecampion, and J. Desroches, Pressure-Driven Suspension Flow Near Jamming, Phys. Rev. Lett. **114,** 088301 (2015).

[12] R. M. Miller and J. F. Morris, Normal stress-driven migration and axial development in pressure-driven flow of concentrated suspensions, J. Non-Newtonian Fluid Mech. **135,** 149 (2006).

[13] L. Isa, R. Besseling, and W. C. K. Poon, Shear Zones and Wall Slip in the Capillary Flow of Concentrated Colloidal Suspensions, Phys. Rev. Lett. **98,** 198305 (2007).

[14] K. Kamrin and M. Z. Bazant, Stochastic flow rule for granular materials, Phys. Rev. E **75,** 041301 (2007).

[15] J. Goyon, A. Colin, G. Ovarlez, A. Ajdari, and L. Bocquet, Spatial cooperativity in soft glassy flows, Nature (London) **454,** 84 (2008).

[16] L. Bocquet, A. Colin, and A. Ajdari, Kinetic Theory of Plastic Flow in Soft Glassy Materials, Phys. Rev. Lett. **103,** 036001 (2009).

[17] O. Pouliquen and Y. Forterre, A non-local rheology for dense granular flows, Phil. Trans. R. Soc. A **367,** 5091 (2009).

[18] K. Kamrin and G. Koval, Nonlocal Constitutive Relation for Steady Granular Flow, Phys. Rev. Lett. **108,** 178301 (2012).

[19] M. Bouzid, M. Trulsson, P. Claudin, E. Clément, and B. Andreotti, Nonlocal Rheology of Granular Flows Across Yield Conditions, Phys. Rev. Lett. **111,** 238301 (2013).

[20] B. Lecampion and D. I. Garagash, Confined flow of suspensions modelled by a frictional rheology, J. Fluid Mech. **759,** 197 (2014).

[21] T. Pähtz, O. Durán, D. N. De Klerk, I. Govender, and M. Trulsson, Local Rheology Relation with Variable Yield Stress Ratio Across Dry, Wet, Dense, and Dilute Granular Flows, Phys. Rev. Lett. **123,** 048001 (2019).

[22] P. Mills and P. Snabre, Rheology and structure of concentrated suspensions of hard spheres. Shear induced particle migration, J. Phys. II (France) **5,** 1597 (1995).

[23] J. F. Morris and F. Boulay, Curvilinear flows of noncolloidal suspensions: The role of normal stresses, J. Rheol. **43,** 1213 (1999).

[24] J. J. J. Gillissen and H. J. Wilson, Modeling sphere suspension microstructure and stress, Phys. Rev. E **98,** 033119 (2018).

[25] J. J. J. Gillissen and H. J Wilson, Effect of normal contact forces on the stress in shear rate invariant particle suspensions, Phys. Rev. Fluids **4,** 013301 (2019).

[26] J. J. J. Gillissen and H. J Wilson, Taylor-Couette instability in sphere suspensions, Phys. Rev. Fluids **4,** 043301 (2019).

[27] J. J. J. Gillissen, C. Ness, J. D. Peterson, H. J. Wilson, and M. E. Cates, Constitutive Model for Time-Dependent Flows of Shear-Thickening Suspensions, Phys. Rev. Lett. **123,** 214504 (2019).

[28] J. J. J. Gillissen, C. Ness, J. D. Peterson, H. J. Wilson, and M. E. Cates, Constitutive model for shear-thickening suspensions: Predictions for steady shear with superposed transverse oscillations, J. Rheol. **64,** 353 (2020).

[29] E. J. Hinch and L. G. Leal, Constitutive equations in suspension mechanics. Part 2. Approximate forms for a suspension of rigid particles affected by Brownian rotations, J. Fluid Mech. **76,** 187 (1976).

[30] When $|\langle q\rangle| \gg q_{\text{rms}}$ we have $\langle|\langle q\rangle + q'|\rangle \approx |\langle q\rangle| \approx |\langle q\rangle| + q_{\text{rms}}$ and when $|\langle q\rangle| \ll q_{\text{rms}}$ we have $\langle|\langle q\rangle + q'|\rangle \approx q_{\text{rms}} \approx |\langle q\rangle| + q_{\text{rms}}$. For the intermediate case $|\langle q\rangle| \sim q_{\text{rms}}$ we interpolate between these limiting cases, giving $\langle|\langle q\rangle + q'|\rangle \approx |\langle q\rangle| + q_{\text{rms}}$.

[31] O. Cheal and C. Ness, Rheology of dense granular suspensions under extensional flow, J. Rheol. **62,** 501 (2018).

[32] To determine β we use that, in the isotropic (microstructure and stress) limit where $\dot{\gamma}_{\text{rms}} \gg \dot{\gamma}$, we have $\xi = \phi/\sqrt{2}$ [28], and demanding jamming at ϕ_{RCP} gives $\xi_J = \phi_{\text{RCP}}/\sqrt{2}$. We furthermore use that, in the simple-shear limit, where $\dot{\gamma}_{\text{rms}} \ll \dot{\gamma}$, we have $\xi = \phi(5\beta^2 - 4\beta + 32)/(2\beta^2 + 8\beta + 64)$ [28], and demanding jamming at ϕ_J gives

$\xi_J = \phi_J(5\beta^2 - 4\beta + 32)/(2\beta^2 + 8\beta + 64)$. Combining these two expressions for ξ_J gives

$$\beta = \frac{\sqrt{200\sqrt{2}\phi_{\text{RCP}}\phi_J - 56\phi_{\text{RCP}}^2 - 156\phi_J^2} - 2\sqrt{2}\phi_{\text{RCP}} - 2\phi_J}{\sqrt{2}\phi_{\text{RCP}} - 5\phi_J},$$

(9)

which is around four for $\phi_{\text{RCP}} = 0.84$ and $\phi_J = 0.795$.

[33] See Supplemental Material at http://link.aps.org/supplemental/10.1103/PhysRevLett.125.184503 for a comparison between constitutive model and discrete element method for flow through curved channel.